IET Journals
The Institution of Engineering and Technology

Survey on Coherent Multiband Splicing Techniques for Wideband Channel Characterization

ISSN 1751-8644
doi: 0000000000
www.ietdl.org

Sigrid Dimce[1], *Falko Dressler*[2*]

[1] *School of Electrical Engineering and Computer Science, TU Berlin, Germany*
** E-mail: {dimce, dresler}@ccs-labs.org*

Abstract: Coherent multi-band splicing is an optimal solution for extending existing band-limited communication systems to support high-precision sensing applications. Conceptually, the communication system performs narrow-band measurements at different center frequencies, which are then concatenated to increase the effective bandwidth without altering the sampling rate. This can be done in parallel for multiple non-contiguous subbands or by hopping across the different bands. However, multi-band splicing poses significant challenges, particularly in compensating for phase offsets and hardware distortions before stitching the acquired samples, which can be distributed in contiguous or non-contiguous manners. In this survey paper, we study the state of the art in coherent multi-band splicing and identify open research questions. For beginners in the field, this review serves as a guide to the most relevant literature, enabling them to quickly catch up with the current achievements. For experts, we highlight open research questions that require further investigation.

1 Introduction

The integration of communication and sensing has recently attracted significant interest in both industry and academia [1]. The main objective of joint communication and sensing (JCAS) is to achieve accurate sensing, by reusing the communication resources. This is both relevant for the widely deployed WiFi infrastructure [2] as well as upcoming 6G networks, which will inherently support JCAS [3]. For example, WiFi devices collect channel state information (CSI), which is extensively utilized for sensing applications. However, in most usage scenarios, bandwidth is limited, and the channel is estimated primarily for equalization purposes without the need for precise multi path component (MPC) parameter estimation [4].

At the same time, sensing applications demand ultra-wideband and highly accurate estimation of MPC parameters, such as delay and amplitude, posing a substantial research challenge for the existing, band-limited infrastructure [4, 5]. One potential solution to virtually increase the bandwidth without changing the sample rate is to use *multi-band splicing*. In the literature, multi-band splicing is also found as channel splicing, or multi-band sensing. This technique *combines* multiple narrow frequency bands to form a wider bandwidth, thereby increasing the channel resolution in the time domain (illustrated in Figure 1).

In principle, the radio system comprising of the transmitter and receiver hops at different center frequencies to perform narrow-band measurements in time domain. The estimated channel frequency responses (CFRs) from each narrow-band measurement are then concatenated in the frequency domain to generate a wider bandwidth and a high-resolution channel impulse response (CIR). The resolution in the delay domain is inversely proportional to the bandwidth ($resolution \sim 1/B$) [6]. This means that higher bandwidth allows for better differentiation between two distinct paths in proximity, as the product of delay resolution and the speed of light determines the necessary separation between paths.

However, there are several challenges associated with the concept of multi-band splicing [1, 4, 7]. Firstly, narrow-band channels might not always be available for sensing due to their potential use by other co-channel devices. As a result, sensing the narrow-band channel before transmission is required, and sequential bands might not always be accessible. Secondly, hardware distortions introduce a phase offset in each narrow-band measurement, making

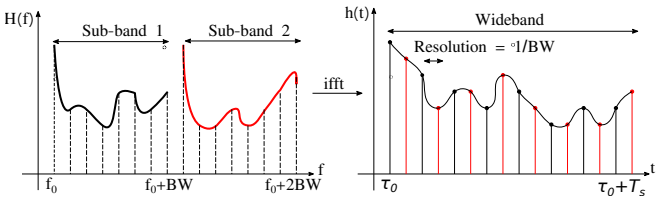

Fig. 1: Illustration of the concept of multi-band splicing

the stitching process on the raw data impossible. Such distortions require overlapped channel measurements to eliminate the issue of the phase offset. Another solution has been identifying each source of the phase offset, estimating and compensating their impact. Thirdly, the channel coherence time limits the number of channel hops or narrow-band measurements that can be conducted. For instance, in an indoor environment at a frequency of 2 GHz, the channel coherence time is several hundred milliseconds when the user is static, and decreases as the user's mobility speed increases. Nevertheless, several works have integrated and applied multi-band splicing, addressing the aforementioned challenges, for applications such as localization [1, 4–6, 8–12], human [13] and respiratory sensing [14, 15].

Based on the way the channel is estimated, a first classification divides the multi-band systems into two groups, *non-coherent* or *coherent* systems [16]. Non-coherent estimators improve channel estimates by averaging the results from all narrow bands. With M narrow bands, the non-coherent estimator [17, 18] averages these estimates from all the M narrow bands to produce a refined measurement. According to Cramer-Rao lower bound (CRLB) [19, 20], the variance of the time-delay error decreases only by a factor M in the non-coherent systems, and by a factor M^3 in the coherent system. Coherent estimators combine simultaneously the estimation results from all the narrow bands, yielding a higher resolution CIR.

In addition to multi-band splicing, alternative approaches are developed to address bandwidth limitations. For example, Wizoom has been introduced [21] using the MUSIC algorithm to estimate the time-delay of the multipath components and combining multiple antennas to improve the resolution. Another approach, detailed in [22], proposes a super-resolution angle of arrival (AoA) algorithm

Table 1 Summary of works on multi-band splicing.

Ref	Application	Frequency	Validation
[1]	localization	2.4 GHz to 7.1 GHz	experimental data
[2]	localization	5 GHz	experimental data
[4]	ranging	6 GHz	simulations and experimental data
[5]	ranging	60 GHz	experimental data
[7]	power delay profile (PDP)	5 GHz	experimental data
[8]	ToA	2.4 GHz and 5 GHz	experimental data
[9]	CIR	-	simulations
[10]	time of arrival (ToA)	2.4 GHz	experimental data
[11]	ToA	3 GHz	simulations
[12]	ranging, ToA	-	simulations
[6]	CIR	2.4 GHz and 5 GHz	simulations
[13]	human sensing	5 GHz	experimental data
[14]	respiration monitoring	5 GHz	experimental data
[15]	respiration monitoring	5 GHz	experimental data
[16]	ToA	802.15.3a/802.15.4a	simulations
[23]	ToA	2.6 GHz	simulations
[24]	CIR	60 GHz	experimental data
[25]	channel reconstruction	28 GHz	simulations
[26]	CSI	2.4 GHz	experimental data
[27]	line of sight (LoS) time-delay	60 MHz, 180 MHz, 290 MHz and 400 MHz	simulations
[28]	ToA	806 MHz/816 MHz	simulations and experimental data
[29]	ranging, CSI	10 MHz, 70 MHz, 130 MHz and 280 MHz	simulations
[30]	ToA	1.8 GHz/2.02 GHz	simulations
[31]	CIR	2.4 GHz	simulations and experimental data
[32]	ranging	5 GHz	simulations
[33]	localization	2.4 GHz, 6 GHz	simulations
[34]	localization	2 GHz	simulations
[35]	localisation	2.4 GHz, 5 GHz	simulations
[36]	ranging	3.5 GHz	experimental data

for decimeter level localization, using multiple APs and the multiple signal classification (MUSIC) algorithm.

Following many theoretical works on channel splicing [6, 9, 16, 23], the concept is now getting more mature and experimental prototypes have been presented. Most of the current research in multi-band splicing is centered around low-frequency bands, i.e., 2.4 GHz and 5 GHz. Only recently, the feasibility to apply the multi-band concept in mmWave frequency bands has been explored [5, 24, 25].

In this survey paper, we review the current state of the art of coherent multi-band splicing techniques. To the best of our knowledge, this is the first paper looking at and offering a summary of the existing research work. We aim to providing a quick get into the concept of multi-band splicing as well as its applications and properties. Furthermore, we give an in-depth description of the hardware distortions and some of the existing approaches in compensating them. We also identify the main observations from all the experimental studies.

The remainder of this paper is organized as follows: Section 2 provides an overview of primary applications of coherent multi-band splicing. A brief description of three methods for delay estimation in multi-band splicing along with an example for each case and an overview on the CRLB is given in Section 3. This is followed by a detailed description of the sources of the hardware distortions and all the proposed techniques for estimating and compensating these errors in Section 4. We discuss open research questions in Section 5. Finally, we conclude this survey in Section 6.

2 Applications

Multi-band splicing is designed to enable communication systems to support sensing functionalities by precisely estimating the CSI. Accurate CSI estimation is essential for enhancing the performance of various sensing applications. Although multi-band splicing has predominantly been used for localization, it has also found applications in channel sounding and human sensing. Table 1 summarizes the state of the art in these areas. In the following, we provide an overview of each application built upon multi-band splicing.

2.1 Ranging and Localization

Over the past two decades, transmitting the same orthogonal frequency-division multiplexing (OFDM) signal over multiple frequency bands to enhance channel estimation for ranging applications has become widespread. The earliest algorithm we could find in the literature that coherently combines contiguous multi-band signals to improve the resolution of ToA estimation is presented in [16]. This algorithm first recovers the CIR with equally spaced taps, then mitigates energy leakage from the first channel path to approximately locate the first path. Its performance is analyzed through simulations and compared with the classical space-alternating generalized expectation-maximization (SAGE) algorithm. An extension of this algorithm is proposed in [23], where non-contiguous, non-equal multiple bands are concatenated to enhance the ToA estimation. Here, cognitive radio is used to sense and select available narrow bands for active range estimation. Performance comparisons between fusion-based and concatenation-based spectra for range estimation show that the concatenated approach offers lower complexity and better performance in resolving closely spaced multipaths.

In [10], the well known indoor localization mechanism, ToneTrack was presented. ToneTrack employs multiple access points (APs) to localize a mobile user, achieving sub-meter accuracy by using contiguous sub-bands and performing amplitude and phase alignment before stitching the spectrum. Subsequently, Chronos [8] was developed, which now allows a single WiFi AP to localize clients to within tens of centimeter, by addressing frequency offset issues between transmitter and receiver and separating time of flight (ToF) from packet detection delay. Another localization technique presented in [9], evaluated through simulations, overcomes the issue of the hardware phase offset by using a phase retrieval scheme that only utilizes the CSI magnitude values to estimate the CIR.

Splicer [7] is a software-based system that splices CSI from multiple contiguous frequency bands to derive high-resolution power delay profiles, focusing particularly on identifying and addressing the source of the hardware distortions within the channel coherence time to support mobility. Integrated into a single AP localization

approach, Splicer achieved a median localization error of $0.95\,\mathrm{m}$. In [11, 27], the authors exploit the multiple shift invariance nature of the Hankel matrices formed from the acquired samples from multiple frequency bands, estimating ToA using the ESPRIT algorithm and the MPC's time-delay using weighted subspace fitting.

In [6], a three step algorithm is proposed for estimating high-resolution CIR for localization purposes. It first performs a per-band processing to estimate and remove linear phase distortions using atomic norm denoising. Then the "clean" samples are concatenated and the sparse recovery orthogonal matching pursuit (OMP) algorithm is applied to estimate the high resolution CIR. Finally, a handshaking protocol resolves ambiguity between the communication nodes.

Moving away from compressed sensing, in [28] an evolution of the SAGE algorithm for the multi-band cases is proposed, exploiting multiple LTE signals simultaneously received on different frequency bands from the base station. A mechanism performing blind joint calibration of multi-band transceivers and time-delay estimation of the MPCs is given in [29], formulated as a covariance matching problem, solved using a group Lasso algorithm. An extension of the algorithm in [27] for solving the multiple shift-invariance nature of the Hankel matrices is presented in [4], acquiring CSI samples from arbitrary frequency bands. CRLB is derived as a benchmark to study the algorithm performance. A two-stage delay estimation technique is developed and enhanced over the years, using non-continuous frequency bands [30, 33–35, 37]. The first stage of the algorithm produces a coarse estimate of the scattering parameters, which is then followed by a refined stage for precise estimation.

Another approach, detailed in [2], concatenates non-adjacent channels to increase time resolution and accuracy in estimating channel parameters (i.e., AoA, angle of departure (AoD) and ToF), performing localization using a single AP and a geometry method that uses multipath channel parameters. A two-stage algorithm is proposed in [32], performing indoor ranging using non-contiguous bands at $5\,\mathrm{GHz}$. UWB-Fi [1] is a sensing system that acquires discrete and irregular channel sampling across $4.7\,\mathrm{GHz}$ bandwidth (i.e., $2.4\,\mathrm{GHz}$ to $7.1\,\mathrm{GHz}$) on commodity Wi-Fi hardware. To handle such irregular samples, a deep learning technique is proposed that translates the discrete channel samples to high-dimensional spectral parameters.

HiSAC [5], is e recently developed JCAS system that combines diverse subsystems and technologies (i.e., 5G-NR and WiGig) and non-contiguous frequency bands to achieve passive ranging. Unlike the aforementioned works operating at low frequencies ($2.4\,\mathrm{GHz}$ to $7.1\,\mathrm{GHz}$), HiSAC operates at $60\,\mathrm{GHz}$, achieving a 20-fold improvement in resolution compared to single-band scenarios.

2.2 Respiration monitoring and human sensing

Channel switching and aggregation to increase the effective bandwidth has been utilized in applications such as respiration monitoring [14, 15] and human sensing [13]. CSI is prone of the environmental changes, making it useful for capturing human activities. In [13] the authors introduce WiRIM, a mechanism for human sensing. WiRIM consists of three steps. First, it employs an algorithm for channel switching and aggregation. Next, the captured CSI is used to construct feature images that contain rich frequency, temporal and spatial characteristics. Finally, a deep learning method processes the extracted features. WiRIM can recognize human activity (i.e., walking, running, sitting, standing activity, picking), even with slight changes in human location. Experimental comparison with another existing approach for human activity recognition and show 96.4% recognition accuracy, compared with 88.6% from the state of the art.

The authors in [14, 15] apply multi frequency bands concatenation to increase the temporal resolution for monitoring respiration. RespiRadio [15] is a respiration monitoring mechanism that utilizes multi-frequency bands with commercial off-the shelf (COTS) WiFi based devices, achieving an overall estimation error of $0.152\,\mathrm{bpm}$. ExRadio [14] is another mechanism that performs real-time respiration monitoring using COTS devices for high dynamic environment. To eliminate the challenge of the hardware-related noises, an additional wire direct connect in constructed. Experiments show that ExRadio achieves an overall detection error of less than $0.5\,\mathrm{bpm}$ in a high dynamic environment, outperforming RespiRadio under the same conditions.

2.3 Channel sounding

Channel sounding, or PDP derivation, is yet another application targeted by multiband sensing. In [26], the authors propose a calibration scheme for both linear and non-linear CSI phase errors, applying this scheme in CSI splicing to generate accurate PDPs. In [24], the authors present mmSplicer, a channel sounder at $60\,\mathrm{GHz}$, that leverages multi-band splicing and sparse recovery techniques for scanning the communication channel. The system utilizes universal software radio peripheral (USRP) software defined radio (SDR) components, and aims estimating a wide channel using only 50% of the narrow frequency bands, to address the issue of the channel coherence time in high frequencies. A multi-band channel reconstruction scheme is presented in [25], for time division duplex (TDD) wideband mmWave multiple-input multiple-output (MIMO) systems under hybrid analog/digital architecture. This approach leverages spatial reciprocity across different frequency bands, requiring only the central sub-band channel to be estimated. The side sub-band channels are then extrapolated from the central one, accompanied by a low-complexity path gain estimation process. To the best of our knowledge, this is the first study to apply multi-band sensing within a MIMO system.

3 Multi-Band Splicing Algorithms

Many studies have attempted to address the challenge of coherent multi-band delay estimation. These existing techniques can be categorized into three main approaches [30]: maximum likelihood-based methods, subspace-based estimation methods, and compressed sensing techniques. Below, we first provide the necessary theoretical background and then a brief overview of each category along with an example algorithm from each. Table 2 provides a short summary of each approach, along with the corresponding pros and cons.

3.1 Theoretical Background

Most experimental research has utilized multi-band splicing within the existing Wi-Fi infrastructure, leveraging the IEEE 802.11 standard and OFDM waveforms to conduct measurements. Therefore, in the following, we assume a 802.11 OFDM communication system, comprised of a transmitter and a receiver, communicating over M frequency bands, each with N subcarriers. The received signal can be expressed as [6]:

$$y[m,n] = H[m,n]S_{m,n} + z[m,n], \quad m \in [M], \quad n \in \mathbb{N},$$

where $S_{m,n}$ is the symbol transmitted over the n-th subcarrier of subband m. For simplicity, we assume that the symbol $S_{m,n} = 1$. $H[m,n]$ represent the CFR characterizing the channel in the frequency domain, and $z[m,n] \sim \mathcal{CN}\left(0, \frac{1}{\mathrm{SNR}}\right)$ stands for the additive white gaussian noise (AWGN). According to the literature [6, 26, 38], the CFR in a multipath environment is given as:

$$H[m,n] = \mathcal{F}\{h(\tau)\}\big|_{f=f_{m,n}} = \sum_{k=1}^{K} c_k e^{-j2\pi f_{m,n}\tau_k}, \quad m \in [M], \quad n \in \mathbb{N}, \tag{1}$$

where K is the number of multipath components, $\tau_k \in [0, \frac{1}{f_s})$ and $c_k \in \mathbb{C}$ are the delays and gain for each path k, and f_s is the subcarrier spacing. The CFR being a complex value, can be expressed in terms of amplitude and phase. Figure 2a depicts an example of a measured CFR, with channel bandwidth $B = Nf_s$. In case of a single antenna device the CSI is equivalent to the CFR, whereas in MIMO system, the CSI is represented as a set of CFR matrices, providing the frequency response between each transmit/receive antenna pair.

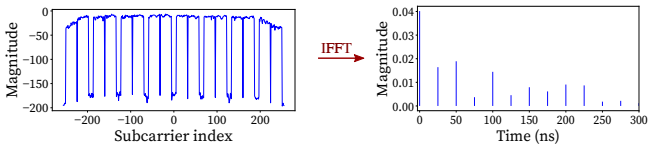

(a) Measured CFR (b) Measured CIR

Fig. 2: CIR and CFR in an OFDM system.

The CIR, characterizing the channel in time domain, is obtained transforming the CSI by inverse fast Fourier transformation (IFFT) (as shown in Figure 2), and is represented as:

$$h(\tau) = \sum_{k=1}^{K} c_k \delta(\tau - \tau_k), \tag{2}$$

where $\delta(\cdot)$ stands for the Dirac's delta function. Figure 2b shows the CIR obtained from the IFFT transformed CFR, with time resolution $\Delta\tau = 1/Nf_s = 1/B$. This relation indicates that larger channel bandwidth leads to higher resolution CIR.

Two multipath components with propagation delays, respectively, τ_1 and τ_2, are indistinguishable in the receiver if $|\tau_1 - \tau_2| < 1/B$. For instance, a channel bandwidth of 20 MHz leads to a time resolution of 50 ns, allowing to distinguish paths that are coming 15 m apart. This distance difference is large for applications such that localization and object mobility tracking.

The received signal in a communication system is subject to several phase distortions due to the hardware imperfections. Section 4 provides a detailed description of the sources of phase distortion in the receiver chain and the existing methods to address them. The phase term from these distortions can be represented as:

$$\psi[m,n] = -2\pi(\delta_m n f_s + \phi_m), \quad m \in [M], \quad n \in \mathbb{N}, \tag{3}$$

where $\delta_m \in \left[0, \frac{1}{f_s}\right)$ depicts the receiver timing offset due to the packet detection delay (PDD) and the receiver sampling frequency offset (SFO). The phase offset term $\phi_m \in [0, 1)$ accounts for the effect of the random phase offset introduced by the phase-locked loop (PLL) when hopping to different frequency bands, along with the accumulated phase offset due to the channel frequency offset (CFO) between the transmitter and receiver. According to [6], δ_m and ϕ_m differ from band to band, making $\psi[m,n]$ a piecewise linear function. On each band, it is a linear function of the subcarrier index with different slope and constant terms. Including the phase distortion, the expression of the received signal can be transformed to [6, Eq. 5]:

$$\begin{aligned} y[m,n] &= e^{j\psi[m,n]} H[m,n] + z[m,n] \\ &= e^{j\psi[m,n]} \sum_{k=1}^{K} c_k e^{-j2\pi f_{m,n}\tau_k} + z[m,n] \\ &= \sum_{k=1}^{K} c_k e^{-j2\pi(f_{m,0}\tau_k + \phi_m)} e^{-j2\pi n f_s(\delta_m + \tau_k)} + z[m,n], \end{aligned}$$

where $f_{m,0}$ is the center frequency of band m. Assuming that the subcarrier spacing is equal, it can be written: $f_{m,n} = f_{m,0} + nf_s$. Given the noisy distorted signal, direct concatenation of samples over different frequency bands is not feasible, hence addressing the challenge of phase distortion is crucial.

3.2 Maximum Likelihood-based Methods

The classical approach for estimating delay parameters typically involves maximum likelihood (ML)-based methods. Consider the following received signal [39]:

$$x[n] = A + w[n], \quad n = 0, 1, ..., N-1, \tag{4}$$

where A is the unknown parameter to be estimated and $w[n]$ is the white Gausian noise. To estimate A using ML, we first determine the probability density function:

$$L(A) = p(x, A) = \frac{1}{(2\pi A)^N/2} exp[\frac{-1}{2A} \sum_{n=0}^{N-1} (x[n] - A)^2] \tag{5}$$

This expression represents the likelihood function as a function of A. Differentiating the log-likelihood function produces: $\frac{\partial p(x,A)}{\partial A}$. The goal is to find the value of A that maximizes the likelihood function, denoted as:

$$\hat{A} = \arg\max_{A} L(A) \tag{6}$$

However, for a set of parameters, solving the ML problem directly can be challenging due to the large dimensionality of the search space. In such cases, the SAGE algorithm is often employed. The SAGE algorithm is preferred as it decomposes the problem into smaller, more manageable subproblems.

In [28], a SAGE-based solution is proposed for estimating the ToA in the downlink LTE networks. However, as noted in [16], a key drawback of the ML algorithms (including SAGE), is their tendency to converge to the local optima. To address this issue, the authors propose a model for estimating the ToA based on equally spaced taps and mitigation of energy leakage from the first channel path. Yet, the estimation of the first path's delay remains coarse, and leads to limited performance improvement.

To overcome the local optima issue, a two stage estimation scheme as been introduced [30, 34]. The two-stage global estimation technique (TSGE) method aims to enhance the estimation accuracy in ToA-based location systems, in the presence of the hardware distortions, leveraging multi-band splicing. The algorithm is designed for a single-input single-output (SISO) system transmitting an OFDM signal over M frequency bands, each with N_m orthogonal subcarriers and f_s subcarrier spacing. The TSGE method consists of two stages:

Stage 1: Coarse estimation using Turbo-BI algorithm In the first stage, the authors construct the coarse signal model from the original signal to reduce complexity and address the issue of local optima (refer to [30, Eq. 4]). The sparse representation of the signal in the delay domain is then used with the turbo Bayesian inference (Turbo-BI) algorithm. The proposed Turbo-BI algorithm exchanges information between the sparse recovery (estimating the significant paths) and the channel estimation, iteratively refining the delay estimates.

Stage 2: Refined Estimation using particle swarm optimization-least square (PSO-LS) In the second stage, a refined delay estimation is performed within a smaller search space, enhancing the computation efficiency. Particle swarm optimization (PSO) is first used to explore the search space for global optimization. Subsequently, a least square (LS) algorithm minimizes the error between the observed and predicted CSI, given the delay estimates from PSO.

An enhanced version of the algorithm was later developed [33, 35, 37]. The algorithm again is composed of two stages. In the first stage, a coarse signal model is derived and the weighted root-MUSIC (WR-MUSIC) algorithm along with the LS method, is used to obtain an initial estimation of the amplitude and delay of the scattering coefficients. A range of the refined estimation is determined using the empirical error from the first stage. In the second stage, a refined signal model and a stochastic particle-based variational Bayesian inference (SPVBI) algorithm is applied for the final parameter estimation.

3.3 Subspace-based Estimation Methods

An alternative approach for estimating the MPC's time-delay using multi-band splicing involves subspace-based methods. In [10],

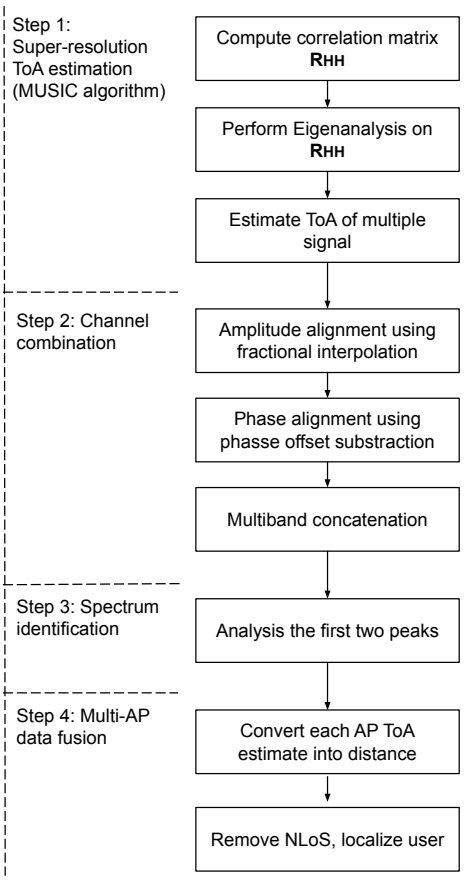

Fig. 3: Block diagram of the ToneTrack algorithm [10].

the authors present ToneTrack, which employs the classical MUSIC algorithm to estimate the time-delays by analyzing the correlation between incoming signals on different subcarrier in frequency domain. However, the presence of multiple shift-invariance structure in the Hankel matrices formed by stitching the multi-band CSI measurements has been identified [4, 11, 27]. These works propose an algorithm that leverages this property and improve the performance. Nonetheless, it has been highlighted in [40, 41] that the subspace estimation methods perform well only with large number of snapshots.

In more detail, the ToneTrack [10] system aims estimating the location of a mobile user using multiple APs. The system is comprised of the following steps: super-resolution ToA processing, channel combination, spectrum identification, and multi-AP data fusion, illustrated in Figure 3. These steps are realized as follows:

Super-resolution ToA estimation ToneTrack uses the MUSIC algorithm, typically known as a super-resolution algorithm. While traditionally applied to time-domain samples, [10] adapts it in frequency domain. Per subcarrier channel response in the frequency domain is expressed as (see [10, Eq. 2]):

$$\mathbf{H}[f_n] = \sum_{k=1}^{D} \alpha_k e^{-j2\pi(f_0+n\Delta f)\tau_k}. \tag{7}$$

where D is the number of the MPCs, f_n and Δf stand for the carrier frequency and the subcarrier spacing, respectively. The estimated channel response $\hat{\mathbf{H}}[f_n]$, from the 802.11 long training field, is used to compute the subcarrier correlation matrix R_{HH}, capturing the phase changes between different subcarriers, as follows:

$$\mathbf{R_{HH}} = E\{\hat{\mathbf{H}}[f_n]\hat{\mathbf{H}}^*[f_n]\} \tag{8}$$

where the expectation is taken across multiple OFDM symbols in time. With N subcarriers, which is larger than the number of the MPCs, the Eigenanalysis of the matrix $\mathbf{R_{HH}}$ results in N Eigenvalues. The eigenvalues are sorted in a non-decreasing order, and then are classified into noise (M-D Eigenvalues) and signal subspace (D Eigenvalues). Next, a time steering vector $\mathbf{a}(\tau)$ in the signal subspace, is defined as (see [10, Eq. 5]):

$$\mathbf{a}(\tau) = \begin{bmatrix} 1 \\ \exp(-j2\pi\tau\Delta f) \\ \vdots \\ \exp(-j2\pi(N-1)\tau\Delta f) \end{bmatrix} \tag{9}$$

where τ represents the MPC time-delays. Finally, the time of arrival of the multiple signals is computed as:

$$\mathbf{P}(\tau) = \frac{1}{\mathbf{a}(\tau)^H \mathbf{E}_N \mathbf{E}_N^H \mathbf{a}(\tau)} \tag{10}$$

where $P(\tau)$ generates peaks when the steering vector is orthogonal to the noise subspace, indicating the arrival times of incoming signals.

However, the MUSIC algorithm struggles resolving paths with small time-delay differences. It has been shown that the resolution still depends on the background noise and the frequency bandwidth of the transmission [10].

Channel combination To overcome the resolution limitation of the MUSIC algorithm, ToneTrack combines multiple frequency bands to virtually form a wider bandwidth. In order to perform multi-band concatenation, first, time and frequency alignment is applied in the collected samples. Amplitude alignment uses fractional interpolation methods to match peaks across spectra, aligning sub-carrier phases and ensuring consistent phase measurements. Frequency domain alignment involves estimating the phase of the last subcarrier of the first channel and aligning the first subcarrier of the second channel by subtracting the phase offset.

Spectrum identification For accurate ToA estimation, spectrum identification isolates and analyses the first two peaks. If the distance between these peaks is larger than the resolution limits than the estimation from MUSIC algorithm is considered correct, otherwise further investigation is necessary. Peaks amplitude are observed: In case the amplitude of the first peak is stronger than the reflection signal then the direct path position is more accurate. If this condition is not fulfilled and the first peak is a merged peak, then the direction of the peak's skew is analysed. If the direction if the peak's skew merges towards the direct path, only then the algorithm proceeds to the last step.

Multi-AP data fusion In the final step, ToneTrack uses the ToA estimations from each AP, and converts them to distance differences to correctly identify the location of the user. The system applies triangle inequality, clustering and outlier rejection, to identify and remove the non-line of sight (NLoS) scenarios. The user's location can be determined from the intersection of the hyperbolas formed by each AP-user pair.

3.4 Compressed Sensing-based Methods

Compressed sensing (CS) aims recovering signals from fewer measurements than the Nyquist rate, under the assumptions that the signals are sparse, meaning that only a few coefficients are non-zero or close to zero [42]. Research has demonstrated that the wireless multipath channel [43], specially in ultra-wideband (UWB) [44] and OFDM [45] systems, exhibit sparsity, making CS applicable for time-delay estimation. Inspired by this concept, several studies leverage CS for time-delay estimation in a multi-band system [5, 6, 8, 9, 24, 25, 31, 32, 36] .

For instance, Chronos [8] is an algorithm that computes the ToF using multi-band splicing and sparse recovery techniques. Yet, requiring a substantial number of bands for optimal performance. A sparse signal for ranging is estimated using the l_i norm in [36] and multiple sparse located signal bands. In [32], a two-stage ToF estimation algorithm is introduced. The first stage uses the sparsity of

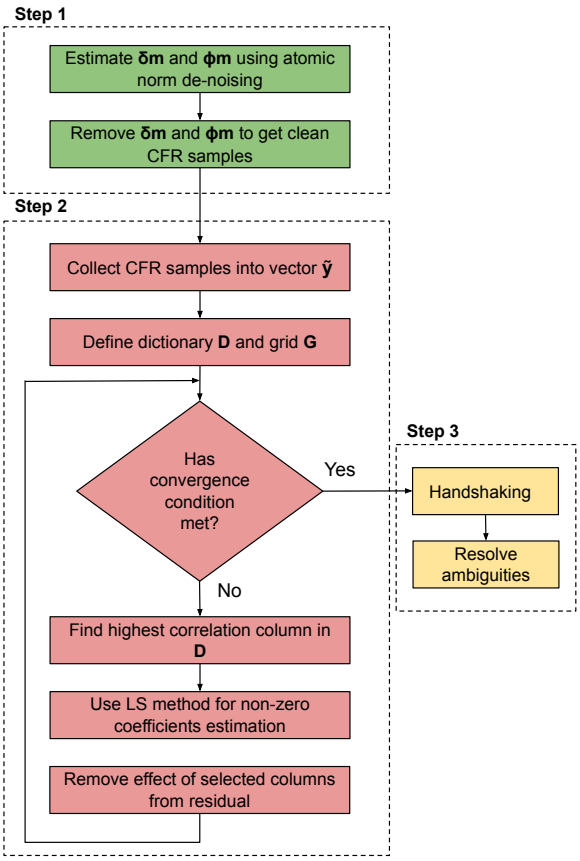

Fig. 4: Flowchart of the compressed sensing algorithm [6].

the CIR to solve the inverse inverse non-uniform discrete Fourier transform (INDFT) for converting CSI samples to CIR. The second stage employs OMP concept to extract ToF. In [6, 9], the OMP grid-based sparse recovery technique is utilized to estimate the full CIR. Despite it low complexity, this method has only been validated through simulations. Nevertheless, the algorithm was successfully integrated into a real communication system and validated it with indoor experimental data [31]. Additionally, OMP was extended into a two stage multi-band splicing technique for scanning the mmWave channel [24]. Finally, HiSAC [5] is a multi-band JCAS system that combines subbands across wide frequency range to achieve high resolution passive ranging, and uses the grid-based OMP algorithm for time-delay and amplitude estimation. In the scope of mmWave MIMO, the authors in [25] propose the beam training-based Newtonized OMP (BT-NOMP) algorithm, which combines the principles of beamtracking with the NOMP algorithm, which is an extension of the OMP method, enhanced for beamforming operation.

Describing multi-band splicing in more detail, we focus on the algorithm presented in [6], which illustrates the use of compressed sensing in multi-band splicing. It involves three steps to recover the wide CIR by combining multiple consecutive frequency bands. The flowchart of the algorithm is presented in Figure 4. Different colors are utilized to represent the different steps of the algorithm.

Step 1: The first step estimates and removes the distortion parameters δ_m, ϕ_m for each frequency band $m \in [M]$, as depicted in Equation (3). Here, δ_m denotes the timing offset due to the PDD and SFO, and ϕ_m represents the phase offset from the CFO and PLL; a detailed description of each source of offsets is provided in Section 4. Hardware imperfections introduce a time and phase offset, which must be estimated and compensated before the CFR samples acquired from different frequency bands are concatenated. The authors use the sparse recovery technique of atomic norm de-noising to estimate these parameters, providing "clean" CFR samples for the next step.

Step 2: The second step employs the OMP greedy algorithm, known for its low complexity and its iterative manner in recovering the sparse signal. The signal can be represented in the following form:

$$\tilde{\mathbf{y}} \approx \mathbf{D}\mathbf{h}_0 + \tilde{\mathbf{z}} \tag{11}$$

where

(a) $\tilde{\mathbf{y}}$ is a vector containing the CFR samples for all the bands, $\tilde{\mathbf{y}} = [\tilde{\mathbf{y}}(1)^T, ..., \tilde{\mathbf{y}}(M)^T]^T \in \mathbb{C}^{MN}$. In the case when only a set of subchannels are used, then the rest of the entries are defined as zero.
(b) a uniform grid of size G is defined over the delay domain as $\mathcal{G} = \{0, 1/G, ..., G-1/G\}/f_s$, and a dictionary $\mathbf{D}$ as $\mathbf{D} = [\mathbf{d}(0), ..., \mathbf{d}(G-1)] \in \mathbb{C}^{MN \times G}$, where $G \gg MN$ and each column $\mathbf{d}(i)$ given as

$$\mathbf{d}(i) = \frac{1}{\sqrt{MN}}[e^{-j2\pi[\mathbf{f}]_1(\frac{i}{G})/f_s}, ..., e^{-j2\pi[\mathbf{f}]_{MN}(\frac{i}{G})/f_s}]^T \in \mathbb{C}^{MN}, \tag{12}$$

where $i = 0, 1, ..., G-1$. In practice the grid is required to be sparse, in the range $G = 2MN$ or $G = 3MN$.
(c) $\tilde{\mathbf{z}}_i$ represents the AWGN
(d) $\mathbf{h}_0 \in \mathbb{C}^G$ is the estimated CIR using the OMP sparse recovery method and the given $\tilde{\mathbf{y}}$ samples.

OMP selects a column of the dictionary $\mathbf{D}$, at each iteration, such that it has the highest correlation with the current residual and it repeats until a convergence condition is met. For each selected column, the non-zero coefficients are computed using the least-square method, such that they approximate the measurement vector $\tilde{\mathbf{y}}$. This step defines the matching part of the OMP algorithm. The effect of each selected column has to be removed from the residual, such that it can not be selected again, and this defines the orthogonality of the OMP method [42]. The algorithm stops once the number of the selected dictionary columns reaches the sparsity order of $\mathbf{h}_0$, which is given as input.

Step 3: The third step addresses the issue of ambiguity, causing a circular shift of the CIR over the delay domain and a global phase shift in the coefficients. An illustration of the ambiguity concept is given in Section 4.2. In order to resolve ambiguities the authors propose a handshaking procedure, during which they exploit the fact that the zero subcarrier in each band is only affected by the phase offset ϕ_m indicating the CFO and the PLL phase offset. This component is constant but has different signs on the transmitter and receiver side, assuming channel reciprocity:

$$y_{\text{tx}}[m, 0] = e^{j\phi_m} H[m, 0] + z_{\text{tx}}[m, 0] \tag{13}$$

$$y_{\text{rx}}[m, 0] = e^{-j\phi_m} H[m, 0] + z_{\text{rx}}[m, 0], \tag{14}$$

During the frequency hopping procedure, the receiver collects for each band the $y_{\text{tx}}[m, 0]$ and $y_{\text{rx}}[m, 0]$, and then multiplies them to obtain the squared CFR samples in the zero subcarrier for each band. Next using the relative CIR estimated from the previous step and an optimization function, the correct ToF is estimated.

3.5 Cramer-Rao Lower Bound

Many studies derive the CRLB as a benchmark to evaluate the performance of developed algorithms, primarily in estimating the ToA [4, 11, 12, 23, 27]. The CRLB represents the absolute lower bound on the variance of an unbiased estimator [23] and is computed as the inverse of the Fisher information matrix (FIM). In [4], the FIM is derived from the partial derivatives of the likelihood function with respect to the delay parameters. The authors aim improving ranging and localization using multi-band CSI. Under certain assumptions, the CRLB for the AWGN channel is expressed in closed form as

Table 2 Summary of multi-band splicing methods.

Method	Summary	Publications	Pros	Cons
Maximum likelihood	Maximizes the likelihood of the observed data for parameter estimation	[16, 28, 30, 33, 34, 37]	1. High precision parameter estimation; 2. Robust to noise	1. Tendency to converge to local optima; 2. High computational complexity
Subspace-based	Utilizes the multi-band signal structure for estimation	[4, 10, 11, 27, 40, 41]	Lower computational complexity	Requires large number of snapshots
Compressed sensing	Exploits the sparse nature of the wireless channel for estimation	[5, 6, 8, 9, 24, 31, 32, 36]	Requires fewer samples than the Nyquist rate	1. Requires dense grids; 2. High computation complexity

(see [4, Eq. 43]):

$$CRB(\hat{\tau}_k) = \frac{1}{2M \cdot \text{SNR}_k}, \tag{15}$$

where M is the number of snapshot measurements. This formula highlights the impact of the number of snapshots and the signal-to-noise ration (SNR) on the CRLB. Similarly, a simplified expression of the CRLB for ToA estimation has been derived [23, Eq. 27]:

$$CRB(\tau_1) = CRB_0 \cdot \frac{1}{1 - \rho^2(|\tau_1 - \tau_2|)}, \tag{16}$$

where CRB_0 is defined as the CRLB for a single reflection and is a function of the center frequency, bandwidth, and SNR, whereas the second term is a function of the time difference between two multi paths (resolution). Based on the CRLB derivations, simulations and experimental data results, the following observations were made:

Frequency aperture: In [4, 23], simulations show the root mean square error (RMSE) of the LoS delay estimation or the variance of the ToA estimation error as a function of SNR, for different frequency band apertures (illustrated in Figure 5). Results indicate that larger frequency aperture outperforms consecutive bands, approaching CRLB. The derivation of CRLB as well depicts that large frequency aperture, higher center frequency, reduce the CRLB, but at low SNR, errors increase with a larger frequency aperture. Furthermore, large frequency aperture can introduce modelling errors due to the frequency dependency of multipath channels. As noted by the authors in [46], the effects of frequency dependence become significant when the frequency band aperture exceeds 20% of the carrier frequency. Additionally, while the impact of frequency aperture has been empirically studied through numerical simulations, it still requires rigorous theoretical analysis.

MPC spacing: In [11] the authors analyze the impact of MPCs spacing in the algorithm performance for different SNR values. The findings suggest that performance is optimal when strong paths are well-separated, but degrades as the paths get closer. Conversely, it was shown that non-continuous subbands yield better results will small subspace, but the performance degrades as the subspace increases [23].

Number of snapshots: The number of CSI snapshots is another factor impacting the algorithm's outcome. As depicted in [4, 27] for a fixed SNR value, the RMSE decreases with the number of snapshots. The authors primarily focus on deriving the CRLB as a metric for delay estimation accuracy.

In [46] the authors study the delay resolution limit in multi-band systems, and introduce another performance metric called the statistical resolution limit (SRL). The SRL is defined as the delay separation that equals its own root squared Cramer-Rao bound:

$$SRL \triangleq \Delta\tau \quad \text{subject to} \quad \Delta\tau = \sqrt{CRB_{\Delta\tau}} \tag{17}$$

Essentially, the delay resolution limit measures the ability to distinguish between two closely spaced signal paths. The numerical results presented in the study reveal the following insights:

(1) As the frequency band aperture increases (i.e., the difference in carrier frequency between adjacent subbands), the SRL decreases, illustrating the frequency band aperture gain in multi-band sensing.

(2) The impact of phase distortion on the SRL is minor and can be mitigated by increasing the frequency band aperture. Yet, the impact of the phase distortion on the delay estimation accuracy remains still unexplored.

(3) A small difference in the amplitude of the scattering coefficients improves the suppression of phase distortion interference.

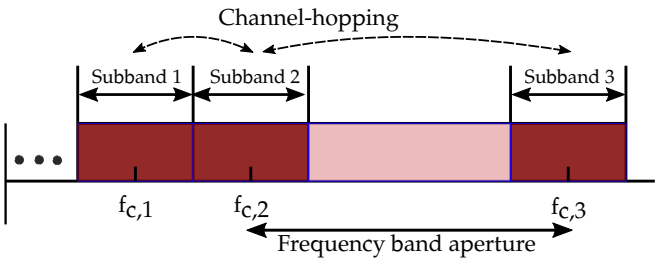

Fig. 5: Frequency distribution in multi-band splicing.

4 Hardware Distortions

Concatenating the acquired CFR samples across multiple frequency bands faces the major challenge of the hardware imperfections, which yield to a time and phase offset for each subband. Therefore, estimating and compensating the offsets is crucial, before stitching the narrow bands to obtain a higher resolution CSI. Various studies have tackled this problem [14, 37, 47], and these approaches can be classified into two categories based on the arrangement of subbands: contiguous [6–10, 26] and non-contiguous [2, 4, 5, 30]. In this section, we first outline the sources of phase errors in the receiver chain and then review how existing research has addressed hardware distortions in both contiguous and non-contiguous subband scenarios.

4.1 IEEE 802.11 Receiver

The 802.11 receiver's chain is comprised of several blocks, as illustrated in Figure 6. The received RF signal is first down-converted to baseband signal $x(t)$, which is next sampled by the analogue to digital converter (ADC) to $x[n]$. The pre-defined 802.11 preamble is used to perform correlation with the received signal $s[n]$ in order to identify the presence of a possible packet. Once a packet is detected, the signal center frequency is calibrated using the CFO estimation and correction block. The calibrated signal is sent for further post-processing, including OFDM demodulation and channel estimation. The estimated CSI is used by the equalization block to compensate the channel impact on the propagating signal. The equalized signal is finally recovered. The blocks in the receiver chain introduces several distortions in the estimated CSI.

Table 3 Summary of amplitude and phase offset compensation techniques, for contiguous subbands scenario.

Technique	Strengths	Weaknesses	Use Cases
Amplitude offset compensation (Averaging CSI measurements)	Frequency independent; Easy to implement	Ineffective in highly dynamic environments, where coherence time is shorter	Suitable when dealing with frequency-independent CSI amplitude errors over coherence time
Non-linear phase error correction (Least square linear fitting or controlled environment)	Corrects the phase offset due to IQ imbalance; The offset is stable over time and RSSI condition	Non-feasible in all the environments	Applicable in the cases when connecting the transmission pair with coaxial cable in feasible, or in a controlled environment
PLL phase offset correction (Handshaking procedure)	Constant term; Exploit the zero subcarrier in each subband	Requires coordination between devices; Complex procedure	Requires a devices with capabilities to switch between Tx/Rx mode
PDD correction (Gaussian distribution modeling)	Averaging over multiple CSI phase; Simple implementation	Requires multiple samples for accurate averaging	Suitable for scenarios where multiple packets are collected
SFO compensation (PDP matching across subbands)	Effective compensation of the clock drifts	Requires careful alignment of the PDP; Assuming clocks offsets are stable during splicing period	Applicable in the cases when the offset is stable during the measurements
CFO compensation (Reference subband)	Frequency independent; Phase of one subband is used for calibration	Small subcarrier spaced systems are more impacted	Applicable in the environments with closely placed subbands
Ambiguities (Handshaking procedure)	Resolving the ambiguities	Requires coordination between devices; Complex procedure	Requires a devices with capabilities to switch between Tx/Rx mode

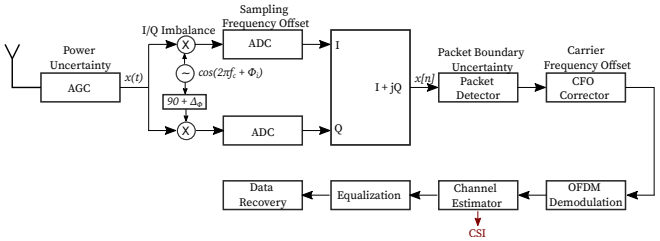

Fig. 6: Illustration of phase error sources in the receiver chain.

4.2 Contiguous Subbands

Several studies apply the concept of multiband splicing over adjacent [8, 10, 17] or overlapping subbands [26]. As with non-adjacent subbands, the impact of the hardware distortions needs to be identified and removed before stitching together samples from all subbands. These distortions can be classified into two main categories: amplitude and phase errors. The latter can be further narrow down into linear and non-linear phase errors. A brief description along with the corresponding sources of these errors, and the proposed solutions, is given below. Furthermore, a summary of all the solution methods, along with their strength, weakness and use cases is provided in Table 3.

4.2.1 Amplitude error: Findings in [7, 26] indicate that CSI traces collected within a frequency band experience an amplitude offset. The root source of the amplitude offset is the power control uncertainty, specifically the automatic gain controller (AGC) in the receiver cannot perfectly compensate the signal amplitude attenuation to the transmitted power level. Consequently, the measured CSI amplitude is the compensated power level, which is mixed with the power control uncertainty error that has to be removed.

Solution: According to [7], the power control uncertainty is frequency independent. Therefore, the author propose averaging all the collected CSI during the channel coherence time, in order to compensate for the amplitude offset.

4.2.2 Non-linear phase error: In theory, the end-to-end Wifi transmission is modeled as a linear system. However, narrow-band measurements (i.e., 20 MHz) conducted over different frequency bands show that the phase of the sub-carriers, particularly at the sides of each band are non-linearly distorted [7, 26]. Recent research [26] has shown that the non-linear CSI phase errors are prevalent within the commodity WiFi devices, and propose that the source of this offset is a consequence of the IQ imbalance from the direct down-conversion in the receiver [48]. A direct conversion receiver employs two quadrature sinusoidal signals for quadrature down conversion. This involves shifting the local oscillator (LO) signal by 90 degrees to generate a quadrature sinusoidal component. If mismatches occur in the gain and phase of these two sinusoidal signals or within the two branches of down-conversion mixers, amplifiers, and low-pass filters, it leads to corruption in the quadrature baseband signals. In the presence of I/Q imbalance, subsequent to sampling and fast Fourier transformation (FFT), the estimated and reported CSI is distorted. The conducted studies have observed that the non-linear phase errors are stable over time and different received signal strength indication (RSSI) conditions, but highly depend of the transmission frequency band.

Solution: Considering that the non-linearity is constant for one device, a possible proposed solution to remove its impact is to measure it off-line and to subtract it in order to obtain linear CSI. The non-linear phase error is measured by connecting the radio chain of the two WiFi devices through a coaxial cable to eliminate the multipath effect. Theoretically, the phase of the sub-carriers changes linearly with its frequency, and the slope is determined by the length of the communication distance d, as [7]:

$$\phi_k = 2\pi \left(f_0 + k\Delta f\right) \frac{d}{c} = \left(2\pi \Delta f \frac{d}{c}\right) k + 2\pi f_0 \frac{d}{c}, \qquad (18)$$

where c is the speed of the signal, k is the subcarrier, Δf stands for the bandwidth of one sub-carrier with frequency $f = f_0 + k\Delta f$.

The authors in [7], utilize a least square linear fitting algorithm through the central sub-carriers (15 to 44), which experience a linear phase to estimate the slope that is used to predict the phase of all the sub-carriers. Next, the non-linearity is computed as the difference between the theoretical linear phase and the measured phase, and then is subtracted in order to generate the linear CSI. The authors claim that the measurements conducted for different devices, reveal that the linear region is in the range of $10\,\mathrm{MHz}$ (sub-carriers 15-44) in the commodity WiFi devices and can reach up to $30\,\mathrm{MHz}$ (sub-carriers 16-112) for WARP software-define-radio.

However, as mentioned in [26], connecting the transmission pair using a coaxial cable, is not always feasible. The authors [26] aim estimating and compensating the following parameters: $\epsilon_{i,A}$ (gain mismatch) and $\epsilon_{i,\Theta}$ (phase mismatch) for a specific band (i) respectively due to the IQ imbalance problem, and ζ (an unknown timing offset). To estimate these parameters, the transmission pair is located in a strong LoS and weak multipath environment.

PLL phase offset: In a system, the PLL is responsible for generating the center frequency for the transmitter and the receiver, starting at a random phase. Hence, jumping at different center frequencies, leads to a random phase offset, which needs to be compensated before splicing the CSI samples.

Solution: The authors in [6, 8] propose a handshaking procedure to eliminate the offset due to the PLL and CFO. According to the authors, the zero sub-carrier in each band is not polluted by any other kind of phase offset, beside the offset induced by PLL and CFO. This constant error term has the same absolute value in the transmitter and the receiver but with different sign, whereas the CFR is the same on both ends due to channel reciprocity. The author exploit this characteristic to multiply the CSI measurements at the receiver and the transmitter, to recover the wireless channel and eliminate the impact of the offset.

4.2.3 Linear phase error: Once the nonlinearity in the CSI phase is estimated and compensated, the residual CSI phase value from any subcarrier $n \in N$ can be expressed as [7, 26]:

$$\phi_n = \theta_n + n \cdot (\lambda_b + \lambda_0) + \beta,$$

where θ_n is identified as the subcarrier phase rotation due to the propagation, λ_b is the phase error coming from the packet detection delay, λ_0 is the phase error caused by the sampling frequency offset, and finally β is the phase error introduced by the central frequency offset. A brief introduction of the source error and the proposed solution of each of the aforementioned components is presented below.

PDD: Once the received signal is downconverted and transformed in the digital domain, using the ADC, the process of packet detection takes place. This process identifies the presence of a packet through energy or correlation detection. Whenever a packet is detected, a time shift (τ_b) is also introduced between the identified starting point of the packet and the ground truth. This time shift is packet-based and leads to a phase rotation error λ_b.

Solution: According to [7], the time shift τ_b, leads to a phase error per subcarrier k: $2\pi k\tau_b/N$, hence the phase shift can be written as: $\lambda_b = 2\pi\tau_b/N$. Considering that the time shift τ_b follows a Gaussian distribution with mean zero, the error λ_b as well follows the same distribution $\lambda_b \sim N(0, \sigma^2)$. Based on the law of large number, to remove the impact of the phase error from the PDD, the authors propose averaging over multiple CSI phases. Nevertheless, according to [26], averaging over a small number of acquired CSI within channel coherence time does not help to get the mean, considering that the variance of distribution is large and leads to a residual phase rotation. The authors combine the phase offset due to the PDD and SFO as one term, following Gaussian distribution. They use overlapping bands and represent the phase error mathematically, solving for the unknown phase offset using ordinary least squares [26, Eq. 6]).

SFO: The sampling frequency offset comes as a result of the mismatch between the sampling interval at the transmitter and that at the receiver [7, 26, 49]. Due to the mismatch, the received signal experience a time shift after the ADC block with respect to the transmitted signal, which translates to a phase rotation λ_0. According to [26], the SFO can be considered nearly constant, since the clock offsets are stable withing short times.

Solution: The authors in [7] express the fractional difference in the sampling frequency between transmitter and receiver as $\zeta = \frac{f_s}{f_r} - 1$. The SFO is defined as $\lambda_0 = \zeta'$, where ζ' indicate ζ multiplied with a constant. Since the clocks offsets are stable in the order of minutes [50], the SFO is considered constant during the process of multiband splicing. To remove the impact of SFO, the authors rely on the assumption that the PDP from different frequency bands should look the same after the SFO is compensated, since the characterized channel is the same. For each frequency band, the CSI phases from all the subcarriers are stacked into a vector. Next for each two bands, the vectors are gradually rotated into the frequency domain, until the PDPs best match each other. The authors define the similarities of two PDPs by computing the power level differences ($P_1 and P_2$) as follows: $\rho(P_1, P_2) = \frac{1}{\|P_1 - P_2\|^2}$. A high value of $\rho(P_1, P_2)$ indicates that the PDPs are similar.

CFO: The carrier frequency offset is a result of the misalignment between the transmitter and receiver's local oscillators. According to [51], factors such as temperature changes and aging, influence the oscillator frequency to drift slowly, resulting in a slowly varying CFO between a communication pair. Even though the CFO estimation and compensation is part of the receiver block, due to these errors this compensation is performed partially leading to a residual phase offset β that is fast time-varying. According to [49], compared to the single carrier systems, OFDM systems are more sensitive to frequency offsets, particularly when using small subcarrier space.

Solution: According to the authors in [7], the CFO is frequency independent, and has no influence in the per-subband derived PDP. Given this observation, they do not derive the CFO β, but when apply the multiband splicing, the phase obtained from any band is used as a reference to calibrate the phases of the other bands.

Ambiguities: The inherent ambiguity is an important factor that influences the correct estimation of the ToF. According to [8], a Δf separation in the frequencies of measured CSI, translates into an ambiguity of multiplies of $\frac{1}{\Delta f}$ in the time domain. To understand the concept of ambiguities, we consider the following example [6]: two CIRs for the same channel are defines as given in Equation (2):

$$h^{(1)}(\tau) = \sum_{k=1}^{K} c_k^{(1)} \delta(\tau - \tau_k^{(1)}) \tag{19}$$

$$h^{(2)}(\tau) = \sum_{k=1}^{K} c_k^{(2)} \delta(\tau - \tau_k^{(2)}), \tag{20}$$

where each CIR comes along with a corresponding set of phase distortion parameters: $\delta_m^i, \phi_m^i,\ i \in \{1, 2\}, m \in [M]$, where in this case δ_m^i denotes the timing offset due to the PDD and SFO, and ϕ_m^i represents the phase offset from the CFO and PLL. Assume the parameters from the two CIRs are related as follows:

$$\begin{aligned} \tau_k^{(2)} &= \tau_k^{(1)} - \overline{\delta}, \\ c_k^{(2)} &= c_k^{(1)} e^{j2\pi\overline{\phi}}, \quad \text{for all } k, \end{aligned}$$

$$\begin{aligned} \delta_m^{(2)} &= \delta_m^{(1)} + \overline{\delta}, \\ \phi_m^{(2)} &= \phi_m^{(1)} + \overline{\phi}, \quad \text{for all } m, \end{aligned}$$

where $\overline{\delta}$ and $\overline{\phi}$ are arbitrary values. In these circumstances, the two received signals will match: $y^{(2)}[m, n] = y^{(1)}[m, n]$ for all m, n.

Table 4 Summary of phase offset compensation techniques, for non-contiguous subbands scenario.

Technique	Strengths	Weaknesses	Use Cases
Phase offset compensation through handshaking procedure	Frequency independent; Hardware imperfections are represented by a single component	Assuming channel reciprocity	Suitable in the cases when channel reciprocity applies
AoA/AoD calibration	Eliminates PLL offset using local calibration RF cables; Reduces complexity by using an additional WiFi card dedicated for calibration	Requires additional hardware (i.e., WiFi card)	Suitable for precise AoA/AoD estimation
ToF sanitation (Linear phase subtracting)	Removes the offset due to symbol timing offset (STO)	Limited to synchronized RF chains	Suitable for ToF estimation in systems with synchronized RF chains
Anchor-based synchronization	Addresses the issue of non-idealises	Requires an anchor path	Applicable in multi-band system

Hence it can observed that it exists two ambiguities when estimating CIR; the first one is a circular shift of the CIR in the delay domain, and the second one is a global phase shift of the CIR coefficients. In the case of ToF estimation, the delay shift is crucial.

Solution: The authors in [6] propose a handshaking mechanism for resolving the ambiguities described in the third step of the algorithm given in Section 3.4.

Other works take different approaches in addressing the impact of the hardware distortions. As described in Section 3.3, ToneTrack performs amplitude and frequency alignment, and it does not take into consideration the impact of ambiguities. In Chronos [8], the authors use the assumption that the zero subcarrier is not impacted by the PDD, hence is identical in phase to the true channel, to resolve the issue of PDD. Furthermore, channel reciprocity is exploit to address the problem of the phase offset. The authors do not consider the issue of ambiguity since it corresponds to a multiply distance of $60\,\mathrm{m}$, which is not typical distance for an indoor environment.

4.3 Non-Contiguous Subbands

Applying the multiband splicing technique over adjacent subbands is not always feasible, as closely spaced channels might be occupied by other applications. In such cases, the amplitude and phase offset can not be removed using the same techniques as in the case the subbands are contiguous. Table 4 summarizes the methods addressing the issue of phase offset in the case of non-contiguous subbands, along with theirs strength, weakness and use cases.

In [4], the authors consider a scenario composed of a mobile node and an anchor. The phase offset from the hardware imperfection is represented by a single component ψ. Assuming that the nodes are not phased synchronized $\psi_{M,i} \not\approx \psi_{A,i}$, then the CSI acquired at the mobile node will look as following: $\boldsymbol{h}_{M,i} = \boldsymbol{\Psi}_i \boldsymbol{h}_i$, where $\boldsymbol{h}_i$ is the CSI vector and $\boldsymbol{\Psi}_i = e^{-j\psi_i}\boldsymbol{I}_N$, where N is the number of the subcarriers, $\boldsymbol{I}_N$ is the NXN identity matrix, and $\psi_i = \psi_{M,i} - \psi_{A,i}$ is the unknown phase offset at the ith carrier frequency. The authors assume that the phase ψ_i remains the same for a fixed carrier frequency, and it has opposite signs when estimated at the anchor and mobile node. Assuming channel reciprocity, one can write the CSI collected at the anchor as following: $\boldsymbol{h}_{A,i} = \boldsymbol{\Psi}_i^* \boldsymbol{h}_i$. Next, the square root of the point-wise product between the collected CSIs is derived as: $\boldsymbol{h}_{D,i} = (\boldsymbol{h}_{M,i} \odot \boldsymbol{h}_{A,i})^{1/2} = \pm \boldsymbol{h}_i$ eliminating the phase offset.

Similarly, in [2] a scenario consisting of an AP and a user is considered. The authors present M^3, a mechanism that performs device localization using the ToF information of the LoS path and the reflection signals. For higher resolution ToF estimation multiple channels are utilized to increase the spectrum. Nevertheless, the issue of the phase offset is addressed before estimating the parameters of AoA,AoD and ToF, as following:

Calibration for AoA and AoD: The PLL generates a phase offset for each RF chain, which does not change unless the WiFi device is reset. To eliminate the PLL offset, the authors use the local calibration technique, where the devices are connected via RF cables to compute the phase offset [2]. A phase matrix is establish, including the phase at each end node and the phase rotation between the antennas, aiming to calibrate the unknown phases at the transmitter and receiver. To reduce the computation complexity, a additional WiFi card is used dedicated for calibration purposes.

Sanitizing ToF: According to [2], the ToF estimation is influenced by the random phase offset due to the STO and PDD. The algorithm applied for the sanitation of the ToF is similar to the one applied in [22]. Considering that all the RF chains in the WiFi card are synchronized, then the STO is the same for all the antennas for a particular subcarrier. The STO is represented as a linear frequency component in the channel's phase response. The authors in [22] show that subtracting the linear fit that is common to the unwrapped phase response of all antennas before estimating multipath parameters removes the variance caused by varying STO.

HiSAC [5] is another mechanism operating on multiple non-contiguous channels, that addresses the issue of unwanted offsets in the receiving signal. These unwanted offsets are specific to a communication pair and are a consequence of the time-varying drifts of the LOs from their normal oscillating frequency, and a random initial offset. The authors categorize them into three main groups: carrier frequency offset, timing offset, and random phase offset. CFO results from time-varying differences between transmitter and receiver local oscillators. Generally, systems attempt to estimate and correct for CFO, but this results in residual errors causing fast-varying CFO, leading to cumulative phase shifts across packets or OFDM slots. Time offset is due to the lack of time synchronization between the communication nodes, and is time-varying causing a phase term that increases linearly with the subcarriers in the case of an OFDM waveform. The random phase offset is a result of the non-idealities in a communication pair and the phase noise. It might be present even between different multibands in the same subsystem LO. In order to achieve phase synchronization between the communication nodes, the authors exploit an anchor path, which is a LoS or NLoS path seen by all the subsystems. The anchor path is used by each subsystem to initialize the time offset accurately, and then compensate for the time offset and phase offset. Nevertheless, the algorithm assumes that the time difference between CFR estimates at different time instances and in different subsystems is short enough to consider the channel parameters to be constant.

5 Open Research Directions

Coherent multi-band splicing is a rather novel technology. The research community has primarily focused on identifying fundamental limitations, such as hardware distortions, subband spacing, and number of snapshots. In the following, we summarize several open challenges and possible future research directions, which are classified into three groups: hardware challenges, antenna beamforming, and algorithm design.

5.1 Hardware Challenges

The issue of the phase offset introduced by hardware distortions has already been studied in the literature with respect to the multi-band splicing systems. Several sources of these distortions are identified and algorithms have been developed to estimate and compensate their impact, before the measurements from different subbands are concatenated. However, the following aspects have not yet been investigated.

Mobility: Mobility and the Doppler effect are another aspect that remain unexplored in multi-band concatenation. Doppler effect introduces additional phase shift in the subbands CFRs, due to the frequency spread. The impact of these shifts on the stitching process has not yet been analyzed.

Phase Noise: When moving to high frequencies, one of the primary challenges is high phase noise [52]. Oscillators at high frequencies exhibit higher noise power spectral density, and the increased bandwidth contributes to phase distortion. Channel coherence time also reduces significantly, becoming a bottleneck for the number of hops and measurements that can be obtained. Further investigations are necessary to study the impact of the phase noise on the performance of the algorithms and the limitations introduced by the coherence time.

5.2 Antenna Beamforming

Most research has concentrated on the frequency range between $2.4\,\mathrm{GHz}$ to $7\,\mathrm{GHz}$, leaving higher frequency bands like $60\,\mathrm{GHz}$ largely unexplored. WiGig, and specifically 802.11ay operates at $60\,\mathrm{GHz}$ and supports $2.16\,\mathrm{GHz}$ bandwidth per band. By combining four channels, it can achieve a total bandwidth of up to 8.64 GHz, reaching cm level resolution. Although a few recent works have focused on high frequencies (i.e., $60\,\mathrm{GHz}$ [5, 24]), many aspects remain under investigated, such as the phase noise and the channel coherence time. While concatenating frequency bands that are very further apart (i.e., sub-$6\,\mathrm{GHz}$ and $60\,\mathrm{GHz}$) is not feasible due to the different signal propagation characteristics, smarter approaches that combines knowledge obtained from the PDP of each frequency bands might be useful. Further research is this direction is strongly required.

Additionally, communication in higher frequency bands is usually linked to beamforming, which is crucial for overcoming high attenuation and extending communication range. However, such antennas are characterized by very narrow beams, which provide a limited view of the environment (mostly LoS component and a very few reflections). In these circumstances, we can distinguish between omnidirectional sensing at low frequencies and non-omnidirectional sensing at millimeter wave frequencies. Non-omnidirectional sensing looks to be particularly interesting for applications such as active ranging and localization, but it is less suitable for human sensing or passive sensing, where a broader characterization of the channel is necessary.

When integrating new technologies such as reflecting intelligent surfaces (RIS) in the communication systems, the system will benefit the splicing concept for calibration of the artificially created multipath environment. The same holds for applications like localization, ranging, and human sensing. Here RIS may help to obtain a wider view on the environment despite very narrowband antennas in mmWave systems.

5.3 Algorithm Design

Despite the enhancements in existing multi-band splicing algorithms, several aspects still require further investigation from our perspective.

Available Bandwidth: As mentioned, multi-band splicing extends a communication system to support sensing applications with high accuracy, such as localization, ranging, and human sensing. To achieve high accuracy, the effective bandwidth is increased virtually by concatenating multiple contiguous or non-contiguous narrowband samples. Existing studies have shown good accuracy results; however, the issue of spectrum availability over time has not been addressed. Considering that the spectrum is shared among several users, the amount of available bandwidth might not always be sufficient for the sensing application to reach the same level of accuracy. None of the existing studies so far have addressed this issue, which requires dynamic adjustments to handle this situation effectively.

Design: One of the main bottlenecks when moving to high frequencies is addressing the data storage issue while providing high accuracy and real time processing. Enhanced models that allow quick measurements throughout several narrow frequency bands, within coherence time, and online postprocess the data, without leading to data storage issues are necessary.

6 Conclusions

Multi-band splicing is gaining increasing attention, particularly with the transition from 5G to 6G and from WiFi6 to WiFi7. By leveraging existing infrastructure, it expands classical communication systems to also support highly accurate sensing applications. Nevertheless, there are still many open questions that need to be investigated to mature the technology. In this survey, we revisited the state of the art in multi-band splicing and highlighted challenges which need to be studied from the research community. We see this survey as a reference for beginners in the field as well as for practitioners who aim using multi-band splicing for sensing applications.

7 References

1 X. Li, H. Wang, Z. Chen, Z. Jiang, and J. Luo, "UWB-Fi: Pushing Wi-Fi towards Ultra-wideband for Fine-Granularity Sensing," in *Annual International Conference on Mobile Systems, Applications and Services (MobiSys 2024)*, Minato-ku, Tokyo, Japan, Jun. 2024, pp. 42–55.

2 Z. Chen, G. Zhu, S. Wang, Y. Xu, J. Xiong, J. Zhao, J. Luo, and X. Wang, "M^3: Multipath assisted Wi-Fi localization with a single access point," *IEEE Transactions on Mobile Computing*, vol. 20, no. 2, pp. 588–602, 2021.

3 T. Wild, V. Braun, and H. Viswanathan, "Joint Design of Communication and Sensing for Beyond 5G and 6G Systems," *IEEE Access*, vol. 9, Jan. 2021.

4 T. Kazaz, G. J. Janssen, J. Romme, and A.-J. Van der Veen, "Delay estimation for ranging and localization using multiband channel state information," *IEEE Transactions on Wireless Communications*, vol. 21, no. 4, pp. 2591–2607, 2021.

5 J. Pegoraro, J. O. Lacruz, M. Rossi, and J. Widmer, "HiSAC: High-Resolution Sensing with Multiband Communication Signals," arXiv, eess.SP 2407.07023, Jul. 2024.

6 M. B. Khalilsarai, B. Gross, S. Stefanatos, G. Wunder, and G. Caire, "WiFi-Based Channel Impulse Response Estimation and Localization via Multi-Band Splicing," in *IEEE Global Communications Conference (GLOBECOM 2020)*. Taipei, Taiwan: IEEE, Dec. 2020.

7 Y. Xie, Z. Li, and M. Li, "Precise Power Delay Profiling with Commodity Wi-Fi," *IEEE Transactions on Mobile Computing*, vol. 18, no. 6, pp. 1342–1355, Jun. 2019.

8 D. Vasisht, S. Kumar, and D. Katabi, "Decimeter-level localization with a single WiFi access point," in *13th USENIX Symposium on Networked Systems Design and Implementation (NSDI 2016)*, Santa Clara, CA, Mar. 2016, pp. 165–178.

9 M. B. Khalilsarai, S. Stefanatos, G. Wunder, and G. Caire, "WiFi-based indoor localization via multi-band splicing and phase retrieval," in *19th IEEE International Workshop on Signal Processing Advances in Wireless Communications (SPAWC 2018)*, Kalamata, Greece, Jun. 2018, pp. 1–5.

10 J. Xiong, K. Sundaresan, and K. Jamieson, "Tonetrack: Leveraging frequency-agile radios for time-based indoor wireless localization," in *21st ACM International Conference on Mobile Computing and Networking (MobiCom 2015)*, Paris, France, Sep. 2015, pp. 537–549.

11 T. Kazaz, R. T. Rajan, G. J. Janssen, and A.-J. Van der Veen, "Multiresolution time-of-arrival estimation from multiband radio channel measurements," in *IEEE*

International Conference on Acoustics, Speech and Signal Processing (ICASSP 2019), Brighton, United Kingdom, May 2019, pp. 4395–4399.
12 M. Pourkhaatoun and S. A. Zekavat, "High-resolution low-complexity cognitive-radio-based multiband range estimation: Concatenated spectrum vs. Fusion-based," *IEEE Systems Journal*, vol. 8, no. 1, pp. 83–92, 2013.
13 X. Shen, L. Guo, Z. Lu, X. Wen, and Z. He, "WiRIM: Resolution improving mechanism for human sensing with commodity Wi-Fi," *IEEE Access*, vol. 7, pp. 168 357–168 370, Nov. 2019.
14 J. Qiu, P. Zheng, K. Chi, R. Xu, and J. Liu, "Respiration Monitoring in High-Dynamic Environments via Combining Multiple WiFi Channels Based on Wire Direct Connection Between RX/TX," *IEEE Internet of Things Journal*, vol. 10, no. 3, pp. 1558–1573, Feb. 2023.
15 S. Shi, Y. Xie, M. Li, A. X. Liu, and J. Zhao, "Synthesizing wider WiFi bandwidth for respiration rate monitoring in dynamic environments," in *38th IEEE Conference on Computer Communications (INFOCOM 2019)*, Paris, France, Apr. 2019, pp. 181–189.
16 H. Xu, C.-C. Chong, I. Guvenc, F. Watanabe, and L. Yang, "High-resolution TOA estimation with multi-band OFDM UWB signals," in *IEEE International Conference on Communications (ICC 2008)*, Beijing, China, May 2008, pp. 4191–4196.
17 C. R. Berger, S. Zhou, Z. Tian, and P. Willett, "Precise timing for multiband OFDM in a UWB system," in *IEEE International Conference on Ultra-Wideband*, Waltham, MA, United States, Sep. 2006, pp. 269–274.
18 R. R. Thomas, B. Zayen, R. Knopp, and B. T. Maharaj, "Multiband time-of-arrival positioning technique for cognitive radio systems," in *22nd IEEE International Symposium on Personal, Indoor and Mobile Radio Communications (PIMRC 2011)*, Toronto, Canada, Sep. 2011, pp. 2315–2319.
19 E. Saberinia and A. H. Tewfik, "Enhanced localization in wireless personal area networks," in *IEEE Global Telecommunications Conference (GLOBECOM 2004)*. Dallas, TX: IEEE, Dec. 2004, pp. 2429–2434.
20 ——, "Ranging in multiband ultrawideband communication systems," *IEEE Transactions on Vehicular Technology*, vol. 57, no. 4, pp. 2523–2530, Jul. 2008.
21 H. Xue, J. Yu, Y. Zhu, L. Lu, S. Qian, and M. Li, "Wizoom: Accurate multipath profiling using commodity wifi devices with limited bandwidth," in *16th IEEE International Conference on Sensing, Communication, and Networking (SECON 2019)*, Boston, MA, Jun. 2019, pp. 1–9.
22 M. Kotaru, K. Joshi, D. Bharadia, and S. Katti, "SpotFi: Decimeter Level Localization Using WiFi," *ACM SIGCOMM Computer Communication Review*, vol. 45, no. 4, pp. 269–282, Sep. 2015.
23 M. Pourkhaatoun and S. A. Zekavat, "Concatenated spectrum multi-band TOA estimation," in *22nd IEEE International Symposium on Personal, Indoor and Mobile Radio Communications (PIMRC 2011)*, Toronto, Canada, Sep. 2011, pp. 1192–1196.
24 S. Dimce, A. Zubow, and F. Dressler, "mmSplicer: Toward Experimental Multi-band Channel Splicing at mmWave Frequencies," in *43rd IEEE International Conference on Computer Communications (INFOCOM 2024), Poster Session*. Vancouver, Canada: IEEE, May 2024.
25 W. Chen, Y. Han, S. Jin, and H. Sun, "Efficient multiband channel reconstruction and tracking for hybrid mmWave MIMO systems," *IEEE Transactions on Communications*, vol. 69, no. 12, pp. 8501–8517, 2021.
26 Y. Zhuo, H. Zhu, H. Xue, and S. Chang, "Perceiving accurate CSI phases with commodity WiFi devices," in *36th IEEE Conference on Computer Communications (INFOCOM 2017)*. Atlanta, GA: IEEE, May 2017.
27 T. Kazaz, G. J. M. Janssen, and A.-J. van der Veen, "Time Delay Estimation from Multiband Radio Channel Samples in Nonuniform Noise," in *53rd Asilomar Conference on Signals, Systems, and Computers*. Pacific Grove, CA: IEEE, Nov. 2019.
28 M. Noschese, F. Babich, M. Comisso, and C. Marshall, "Multi-band time of arrival estimation for long term evolution (LTE) signals," *IEEE Transactions on Mobile Computing*, vol. 20, no. 12, pp. 3383–3394, 2020.
29 T. Kazaz, M. Coutino, G. J. Janssen, and A.-J. Van der Veen, "Joint blind calibration and time-delay estimation for multiband ranging," in *IEEE International Conference on Acoustics, Speech and Signal Processing (ICASSP 2020)*, Barcelona, Spain, May 2020, pp. 4846–4850.
30 Y. Wan, A. Liu, Q. Hu, M. Zhang, and Y. Cai, "Multiband Delay Estimation for Localization Using a Two-Stage Global Estimation Scheme," *IEEE Transactions on Wireless Communications*, vol. 22, no. 12, pp. 9263–9277, Dec. 2023.
31 S. Dimce, A. Zubow, A. Bayesteh, G. Caire, and F. Dressler, "Practical Channel Splicing using OFDM Waveforms for Joint Communication and Sensing in the IoT," arXiv, cs.NI 2305.05508, May 2023.
32 Z. Tian, Y. Ren, Z. Li, and X. Cheng, "Super-Resolution Time-of-Flight Estimation for Ranging via Multi-Band Splicing," in *IEEE Global Communications Conference (GLOBECOM 2023)*, Kuala Lumpur, Malaysia, Dec. 2023, pp. 4656–4661.
33 Z. Hu, A. Liu, Y. Wan, T. X. Han, and M. Zhao, "A Two-Stage Multiband Delay Estimation Scheme via Stochastic Particle-Based Variational Bayesian Inference," *IEEE Internet of Things Journal*, Feb. 2024.
34 Y. Wan, A. Liu, Q. Hu, M. Zhang, and Y. Cai, "A two-stage global estimation scheme for multiband delay estimation in wireless localization," in *IEEE Global Communications Conference (GLOBECOM 2022)*, Rio de Janeiro, Brazil, Dec. 2022, pp. 735–740.
35 Z. Hu, A. Liu, Y. Wan, T. X. Han, and M. Zhao, "A Two-stage Multiband WiFi Sensing Scheme via Stochastic Particle-Based Variational Bayesian Inference," arXiv, eess.SP, Oct. 2023.
36 H. Dun, C. C. Tiberius, C. Diouf, and G. J. Janssen, "Sparse signal bands selection for precise time-based ranging in terrestrial positioning," in *IEEE/ION Position, Location and Navigation Symposium (PLANS 2020)*, Portland, OR, Apr. 2020, pp. 1372–1380.
37 Z. Hu, A. Liu, Y. Wan, T. Q. S. Quek, and M.-J. Zhao, "Two-stage Multiband Wi-Fi Sensing for ISAC via Stochastic Particle-Based Variational Bayesian Inference," in *IEEE Global Communications Conference (GLOBECOM 2023)*. Kuala Lumpur, Malaysia: IEEE, Dec. 2023.
38 T. S. Rappaport, *Wireless Communications: Principles and Practice*. Prentice Hall, 1996.
39 S. Kay, *Fundamentals of Statistical Signal Processing: Estimation Theory*. Upper Saddle River, NJ: Prentice Hall, 1998.
40 C. Stoeckle, J. Munir, A. Mezghani, and J. A. Nossek, "DoA estimation performance and computational complexity of subspace-and compressed sensing-based methods," in *19th International ITG Workshop on Smart Antennas (WSA 2015)*, Ilmenau, Germany, Mar. 2015, pp. 1–6.
41 X. Li and K. Pahlavan, "Super-Resolution TOA Estimation With Diversity for Indoor Geolocation," *IEEE Transactions on Wireless Communications*, vol. 3, no. 1, pp. 224–234, Jan. 2004.
42 E. C. Marques, N. Maciel, L. Naviner, H. Cai, and J. Yang, "A review of sparse recovery algorithms," *IEEE Access*, vol. 7, pp. 1300–1322, Dec. 2018.
43 W. U. Bajwa, J. Haupt, A. M. Sayeed, and R. Nowak, "Compressed Channel Sensing: A New Approach to Estimating Sparse Multipath Channels," *Proceedings of the IEEE*, vol. 98, no. 6, pp. 1058–1076, Jun. 2010.
44 J. L. Paredes, G. R. Arce, and Z. Wang, "Ultra-wideband compressed sensing: Channel estimation," *IEEE Journal of Selected Topics in Signal Processing*, vol. 1, no. 3, pp. 383–395, 2007.
45 J. Meng, W. Yin, Y. Li, N. T. Nguyen, and Z. Han, "Compressive sensing based high-resolution channel estimation for OFDM system," *IEEE Journal of Selected Topics in Signal Processing*, vol. 6, no. 1, pp. 15–25, Sep. 2011.
46 Y. Wan, Z. Hu, A. Liu, R. Du, T. X. Han, and T. Q. Quek, "OFDM-Based Multiband Sensing For ISAC: Resolution Limit, Algorithm Design, and Open Issues," *IEEE Vehicular Technology Magazine*, Jun. 2024.
47 C. Chen, Y. Chen, Y. Han, H.-Q. Lai, and K. R. Liu, "Achieving centimeter-accuracy indoor localization on WiFi platforms: A frequency hopping approach," *IEEE Internet of Things Journal*, vol. 4, no. 1, pp. 111–121, 2016.
48 M. Petit and A. Springer, "Analysis of a Properness-Based Blind Adaptive I/Q Filter Mismatch Compensation," *IEEE Transactions on Wireless Communications*, vol. 15, no. 1, pp. 781–793, Jan. 2016.
49 M. Speth, S. Fechtel, G. Fock, and H. Meyr, "Optimum receiver design for wireless broad-band systems using OFDM. I," *IEEE Transactions on Communications*, vol. 47, no. 9, pp. 1668–1677, Sep. 1999.
50 S. Jana and S. K. Kasera, "On fast and accurate detection of unauthorized wireless access points using clock skews," in *14th ACM International Conference on Mobile Computing and Networking (MobiCom 2008)*, San Francisco, CA, Sep. 2008, pp. 104–115.
51 K. Wu, J. Pegoraro, F. Meneghello, J. A. Zhang, J. O. Lacruz, J. Widmer, F. Restuccia, M. Rossi, X. Huang, D. Zhang, G. Caire, and Y. J. Guo, "Sensing in Bi-Static ISAC Systems with Clock Asynchronism: A Signal Processing Perspective," arXiv, eess.SP 2402.09048, Jun. 2024.
52 M. E. Rasekh, M. Abdelghany, U. Madhowz, and M. Rodwell, "Phase noise analysis for mmwave massive MIMO: a design framework for scaling via tiled architectures," in *53rd Annual Conference on Information Sciences and Systems (CISS 2019)*, Baltimore, MD, United States, Mar. 2019, pp. 1–6.